ROTATIONALLY MODULATED *g*-MODES IN THE RAPIDLY ROTATING *δ* SCUTI STAR RASALHAGUE (*α* OPHIUCHI)[*]

J. D. Monnier[1], R. H. D. Townsend[2], X. Che[1], M. Zhao[3], T. Kallinger[4], J. Matthews[4], and A. F. J. Moffat[5]

[1] University of Michigan Astronomy Department, 941 Dennison Bldg, Ann Arbor, MI 48109-1090, USA; monnier@umich.edu
[2] Department of Astronomy, University of Wisconsin-Madison, Sterling Hall, 475 N. Charter Street, Madison, WI 53706, USA
[3] Jet Propulsion Laboratory, Pasadena, CA, USA
[4] University of British Columbia, Vancouver, BC V6T 1Z1, Canada
[5] Université de Montreéal, C.P. 6128, Succ. C-V, QC H3C 3J, Canada

ABSTRACT

Despite a century of remarkable progress in understanding stellar interiors, we know surprisingly little about the inner workings of stars spinning near their critical limit. New interferometric imaging of these so-called rapid rotators combined with breakthroughs in asteroseismology promise to lift this veil and probe the strongly latitude-dependent photospheric characteristics and even reveal the internal angular momentum distribution of these luminous objects. Here, we report the first high-precision photometry on the low-amplitude *δ* Scuti variable star Rasalhague (*α* Oph, A5IV, 2.18 $M_\odot$, $\frac{\omega}{\omega_c} \sim 0.88$) based on 30 continuous days of monitoring using the *MOST* satellite. We have identified 57 ± 1 distinct pulsation modes above a stochastic granulation spectrum with a cutoff of ∼26 cycles day^{-1}. Remarkably, we have also discovered that the fast rotation period of 14.5 hr modulates low-frequency modes (1–10 day periods) that we identify as a rich family of *g*-modes ($|m|$ up to 7). The spacing of the *g*-modes is surprisingly linear considering Coriolis forces are expected to strongly distort the mode spectrum, suggesting we are seeing prograde "equatorial Kelvin" waves (modes $\ell = m$). We emphasize the unique aspects of Rasalhague motivating future detailed asteroseismic modeling—a source with a precisely measured parallax distance, photospheric oblateness, latitude temperature structure, and whose low-mass companion provides an astrometric orbit for precise mass determinations.

Key words: binaries: close – stars: individual: *α* Oph, Rasalhague – stars: variables: delta Scuti – techniques: photometric

Online-only material: color figure

1. INTRODUCTION

One of the most enduring questions of astronomy is "How do stars work?" Progress over the last century has led to a robust scientific framework that explains the physics of internal stellar structure and also how stars evolve in time. This framework strives to include stars of all types, e.g., low-metallicity stars of the early universe, massive stars that will become supernovae, low-mass brown dwarfs as well as stars like our Sun. As a basic rule, our understanding is strongest and best proven for Sun-like stars and gets shakier and less robust for stars very much different from the Sun. This paper will highlight one critical aspect of stellar structure and evolution, but one that hardly affects our Sun—that of stellar rotation.

Stars in general are probably born with significant angular momentum, but most of them are of low mass (like the Sun) and are "slowed" down by their magnetic winds in the early parts of their lives. On the other hand, most intermediate- and high-mass stars ($\gtrsim 1.5$ solar masses) have weak magnetic fields and do not live very long, thus are often observed to be rotating very quickly. "Rapid rotation" is expected to change the star's luminosity and photospheric temperature distribution (Maeder & Meynet 2000) and also strongly modify the observed surface abundances of various elements (Pinsonneault 1997). For the most massive stars, rotation will partially determine when the stars become supernovae, thus having a crucial impact on how

heavy elements get dispersed into the interstellar medium. For all its importance, the effects of rapid rotation are only vaguely understood and cannot be confidently included in our stellar evolutionary codes. More observations are critically needed to support the recent renaissance in theoretical efforts using analytic calculations and three-dimensional hydrodynamical computer simulations (e.g., Lee & Saio 1997; Townsend 2003; Jackson et al. 2005; Roxburgh 2006; Rieutord 2006; Reese et al. 2008).

Recent breakthroughs in making images of nearby rapidly rotating stars using optical interferometry have coincided with new numerical efforts to simulate the internal stellar structure of these stars (e.g., van Belle et al. 2001; Domiciano de Souza et al. 2003; Monnier et al. 2007; Zhao et al. 2009). Many of the original assumptions that had been adopted are under renewed scrutiny and simple assumptions such as rigid-body rotation and early prescriptions for "gravity darkening" do not seem consistent with new data.

Our group recognized the profound advances made possible by combining the new images of nearby rapid rotators with the asteroseismic constraints (see also Cunha et al. 2007 for general discussion of astereoseismology and interferometry) that can be revealed by the precision photometer onboard the *Microvariability and Oscillations of Stars* (*MOST*) satellite (Walker et al. 2003). We have initially identified two rapidly rotating stars observable by *MOST* with extensive published interferometric data sets: Altair and *α* Oph (Rasalhague). Since there is no analytic theory that can predict the effects of rotation on the pulsational modes of a star spinning at nearly 90% of breakup, we plan to use the known stellar and geometric

---
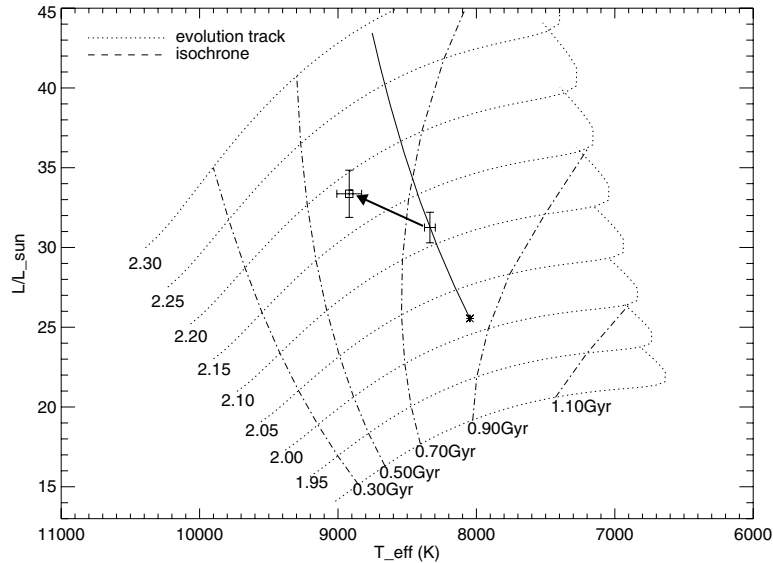
Figure 1. Based on re-analysis of CHARA-MIRC observations originally presented in Zhao et al. (2009), we present a corrected H-R diagram for *α* Oph compared to Y2 isochrones (Yi et al. 2001; Kim et al. 2002; Demarque et al. 2004). The asterisk marks the "apparent" position of *α* Oph, appearing red and faint due to the edge-on viewing angle. The solid line shows the range of possible apparent locations depending on viewing angle with the error bars marking the true luminosity and true effective temperature. Lastly, the square marks the non-rotating equivalent position for *α* Oph to allow comparison to the isochrones.

parameters of our sample to constrain the asteroseismic models with unprecedented power. Essentially, we know everything about the external appearance of these stars (size, oblateness temperature gradients on the surface, viewing angle, rotation periods) from interferometry, and thus, we can use asteroseismic signal for deducing the internal structure without the normally disastrous degeneracies one confronts.

Here, we report on our first results of this project, namely, the oscillation spectrum of *α* Oph using the *MOST* observations as part of the first year NASA Guest Observer program. *α* Oph is classified as an A5IV star (Gray et al. 2001) with an estimated mass of 2.18 $M_\odot$ and is rotating at 88% of breakup as judged by the extreme oblateness of the photosphere observed by interferometry (Zhao et al. 2009). Interferometric imaging also revealed that our viewing angle is nearly exactly equator-on, a perspective that strongly suppresses the photometric amplitudes of $l - |m|$ odd-parity modes, simplifying mode identifications. An early *K* star orbits the primary star with a period of 7.9 years (based on astrometric and speckle data, e.g., Gatewood 2005), which will allow the masses of the two stars to be determined eventually to high precision. Adaptive optics imaging has recently resolved (Hinkley et al. 2010) the two stars and finds the companion to be more than 100× fainter than the primary at wavelengths of the *MOST* instrument and so we have assumed all the pulsation signatures we see are from the primary.

In this paper, we present the full photometric data set for Rasalhague along with an updated stellar model based on interferometry data. We find evidence for both *p*-mode and *g*-mode oscillations along with a remarkable rotational modulation signal. It was beyond the scope of this paper to develop a mode analysis; however, we will pursue this in a future paper.

2. PROPERTIES OF *α* OPH

The physical properties of *α* Oph were recently determined using long-baseline interferometry data from the CHARA Array (ten Brummelaar et al. 2005) using the imaging combiner MIRC (Monnier et al. 2004, 2006). Zhao et al. (2009) reported that *α* Oph was being viewed within a few degrees of edge-on and

with a rotation rate $\frac{\omega}{\omega_{\rm crit}} \sim 88\%$ of breakup assuming a standard Roche model (point mass gravity, solid-body rotation) and a gravity darkening coefficient of 0.25 (von Zeipel 1924a, 1924b).

Since this paper was published, we have slightly improved the calibration and re-analyzed the existing interferometry data. Most importantly, we corrected a methodological error that resulted in inaccurate age and mass when comparing to non-rotating stellar evolution tracks. Figure 1 shows our new estimate of the location of *α* Oph on the Hertzsprung–Russell diagram showing Y2 isochrones (Yi et al. 2001; Kim et al. 2002). We have summarized the new model fits and the stellar parameters in Table 1. Please see Zhao et al. (2009) and X. Che et al. (2010, in preparation) for a detailed description of the model parameters and for details on our fitting methodology.

With the new analysis, we still find *α* Oph to be rotating 88% of breakup (rotation rate of 1.65 c/d) and being viewed within a few degrees of edge-on. However, the derived mass is now a bit higher—2.18 $M_\odot$—a result of the improved isochrone analysis. We will adopt these parameters in discussions throughout the rest of the paper. Note that the error bars in the table rely on fixing the gravity darkening coefficient *β* to 0.25. Evidence is emerging (X. Che et al. 2010, in preparation) that *β* might be substantially lower than this, which could affect the derived stellar parameters.

3. OBSERVATIONS

3.1. Basic Description

The photometry presented here was obtained by the *MOST* satellite. *MOST* houses a CCD photometer fed by a 15 cm Maksutov telescope through a custom broadband optical filter (350–750 nm). The satellite's Sun-synchronous 820 km polar orbit (period = 101.4 minutes = 14.20 cycles day^{-1}) enables uninterrupted observations of stars in its Continuous Viewing Zone ($-18° <$ dec $< +36°$) for up to 8 weeks. A pre-launch summary of the mission is given by Walker et al. (2003) and on-orbit science operations are described by Matthews et al. (2004).

Table 1
Best-Fit and Physical Parameters of α Oph from CHARA-MIRC
Interferometry

Model Parameters	
Inclination (deg)	87.5 ± 0.6
Position angle (deg)	-53.5 ± 1.7
$T_{\rm pol}$ (K)	9384 ± 154
$R_{\rm pol}$ (mas)	0.757 ± 0.004
ω	0.880 ± 0.026
β	0.25 (fixed)
Derived Physical Parameters	
$T_{\rm equ}$ (K)	7569 ± 124
$R_{\rm equ}$ ($R_\odot$)	2.858 ± 0.015
$R_{\rm pol}$ ($R_\odot$)	2.388 ± 0.013
True $T_{\rm eff}$ (K)	8336 ± 39
True luminosity ($L_\odot$)	31.3 ± 0.96
Apparent $T_{\rm eff}$ (K)	8047
Apparent luminosity ($L_\odot$)	25.6
V magnitude[a]	2.087
H magnitude[b]	1.709
$V \sin i$ (km s^{-1})	239 ± 12
Rotation rate (cycles day^{-1})	1.65 ± 0.04
Mass ($M_\odot$)[c]	2.18 ± 0.02
Age (Gyr)[c]	0.60 ± 0.02
χ^2_ν **of Various Data**	
Total χ^2_ν	0.70
CP χ^2_ν	1.08
Vis^2 χ^2_ν	0.86
T3amp χ^2_ν	0.16
Physical Parameters from Literature	
[Fe/H][d]	-0.16
Distance (pc)[e]	14.68

Notes.
[a] V magnitude from literature: 2.086 ± 0.003 (Perryman et al. 1997).
[b] H magnitude from literature: 1.72 ± 0.18 (Cutri et al. 2003).
[c] Based on the Y^2 stellar evolution model (Demarque et al. 2004).
[d] Erspamer & North (2003).
[e] Gatewood (2005).

The *MOST* photometry of the α Ophiuchi binary system covers 30 days during 2009 May 27 to 2009 June 26, and was obtained in Fabry Imaging mode, where the telescope pupil, illuminated by the star, is projected onto the CCD by a Fabry microlens as an annulus covering about 1300 pixels. The data were reduced using the background decorrelation technique described by Reegen et al. (2006). The reduction includes filtering for cosmic particle impacts, correction of the stray light background modulated with satellite orbital parameters, filtering of long-term trends, and removal of obvious outliers.

The final heliocentric corrected time series provided by the *MOST* instrument team contained 81,018 measurements with an exposure time and sampling of 30 s (based on thirty 1 s exposures stacked onboard the spacecraft). The datastream was remarkably consistent and continuous, being on-target with data for about 94% of the α Oph observation. Instrument problems did cause six data gaps in excess of 30 minutes, with the longest being 5 hr.

3.2. Data Reduction

The first step our team applied in our data analysis was to remove local 5σ outliers from the data. Because a similar procedure had already been applied by the *MOST* instrument

team, this step had only a minor effect—reducing the data set to 80,002 independent data points, a data volume reduction of only 1.3%. These flux points are presented in Figure 2 in their entirety.

The next step was to remove the harmonics of the 14.2 c/d orbital period. Similar to the method described by Walker et al. (2005), we used a moving window of 10 days to create a high signal-to-noise mean light curve folded at the orbital period. We then remove this component from the original light curve. The long averaging window ensures we only remove frequencies within a few (Nyquist) resolution elements of the harmonics. We have inspected data both with and without this correction and found the only significant effect was to remove the harmonics from our final power spectra.

Lastly, we "detrended" the light curve in order to filter out slow variations on long timescales. The "slow trend" light curve was constructed by fitting a line segment to the flux measurements (after removal of orbital modulation) within a moving 1-day window. The slow trends were subtracted from the light curve resulting in a final data set on which subsequent Fourier analysis was performed. The slow trend light curve can be seen in Figure 2. At our request, spacecraft telemetry was inspected to see if any camera or telescope diagnostic showed variations in sync with the slow variations seen here—none were found.

We have graphically summarized the steps in our data reduction in Figure 3. Here, we have zoomed up on a single day in our time series and show explicitly the original data, our estimate of the residual orbital modulation, and the slow trend. We also show the final corrected light curve with and without a 5 minutes averaging window to demonstrate the overall quality of our data.

After more than 7 years in orbit, the *MOST* Team has a very robust understanding of the performance of the instrument, especially the point-to-point precision of the photometry as a function of target magnitude and the noise levels at various frequency ranges in Fourier space. Many of the pulsating variable stars detected in the *MOST* Guide Star sample (in the magnitude ranges $6 < V < 10$) had a "discovery amplitude" (i.e., amplitude of the largest oscillation signal) of only about 1–2 mmag, with many other oscillation peaks 10 times smaller and a noise level in Fourier space 50 times lower (e.g., the richly multi-periodic δ Scuti star HD 209775 Matthews 2007). Some examples of stars which characterize the photometric precision of the *MOST* instrument are: HD 146490 (a guide star used as a calibration by Kallinger et al. 2008b; see their Figure 1), with $V = 7.2$ and point-to-point scatter of 0.12 mmag; tau Bootis ($V = 4.5$), an exoplanet-hosting star which shows clear modulation at the planet's orbital period with a peak-to-peak amplitude of 2 mmag (Walker et al. 2008) for which its mean instrumental magnitude is repeatable to within 1 mmag in observations spaced several years apart; and Procyon ($V = 0.35$), with point-to-point precision of 0.14 mmag. In these cases, the noise floor in the Fourier spectrum is well defined and at a level of 0.01 mmag or less.

Another *MOST* target, epsilon Oph (Barban et al. 2007; Kallinger et al. 2008a), a cool giant ($V = 3.24$), is stable to 0.35 mmag at frequencies below 0.1 c/d. At these low frequencies, non-periodic noise intrinsic to the star is usually associated with granulation. The *MOST* Team has never seen instrumental artifacts with the amplitudes and coherence of the variations evident at low frequencies in the *MOST* light curve of α Oph presented here. For the results in this paper,
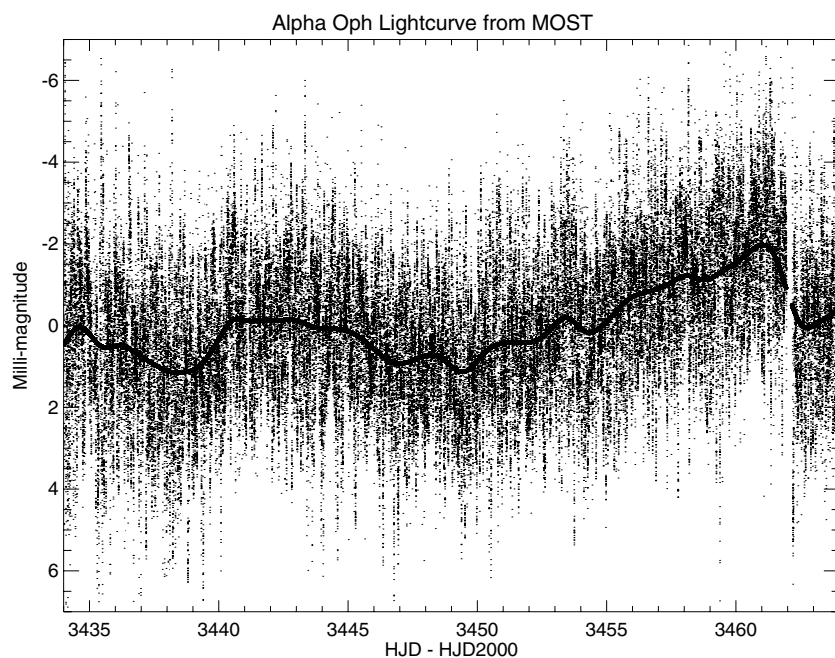
Figure 2. This figure shows the *MOST* photometry of *α* Oph (Rasalhague) in an early stage of data processing. Each tiny point is a measurement over a 30 s period, and the solid line shows the 1 day moving average.
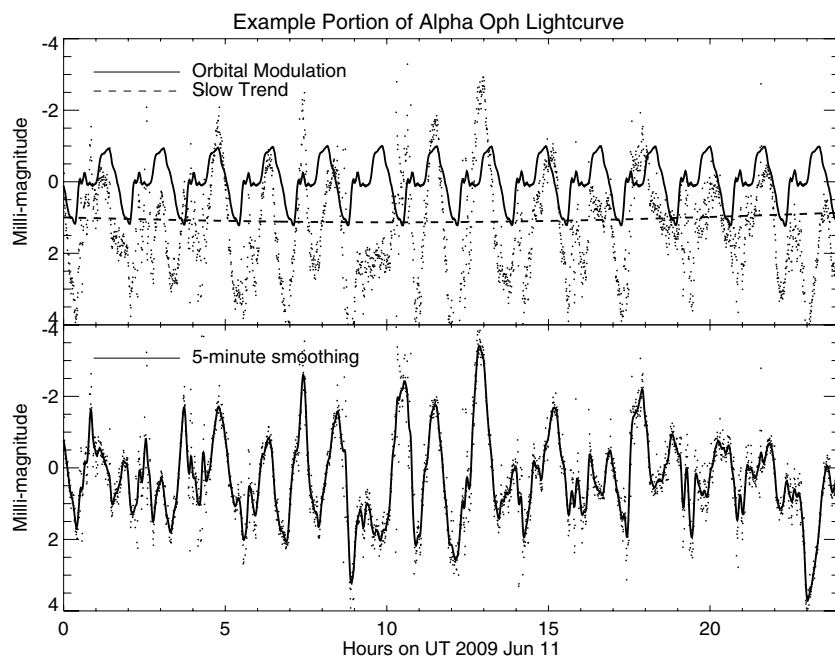
Figure 3. This figure shows each step in the data reduction for the light curve of *α* Oph (Rasalhague). The top panel shows the original data for an example 1 day period along with the estimated orbital modulation and slow trend components. The bottom panel shows the data after removing the orbital modulation and the slow trend—this final reduced light curve was used for Fourier analysis in this paper.

the low-frequency signals have no direct implications, so we do not address them in further detail. However, they are likely intrinsic to the star and hence do not raise any alarms of possible unrecognized photometric artifacts at other frequency ranges in the *α* Oph time series.
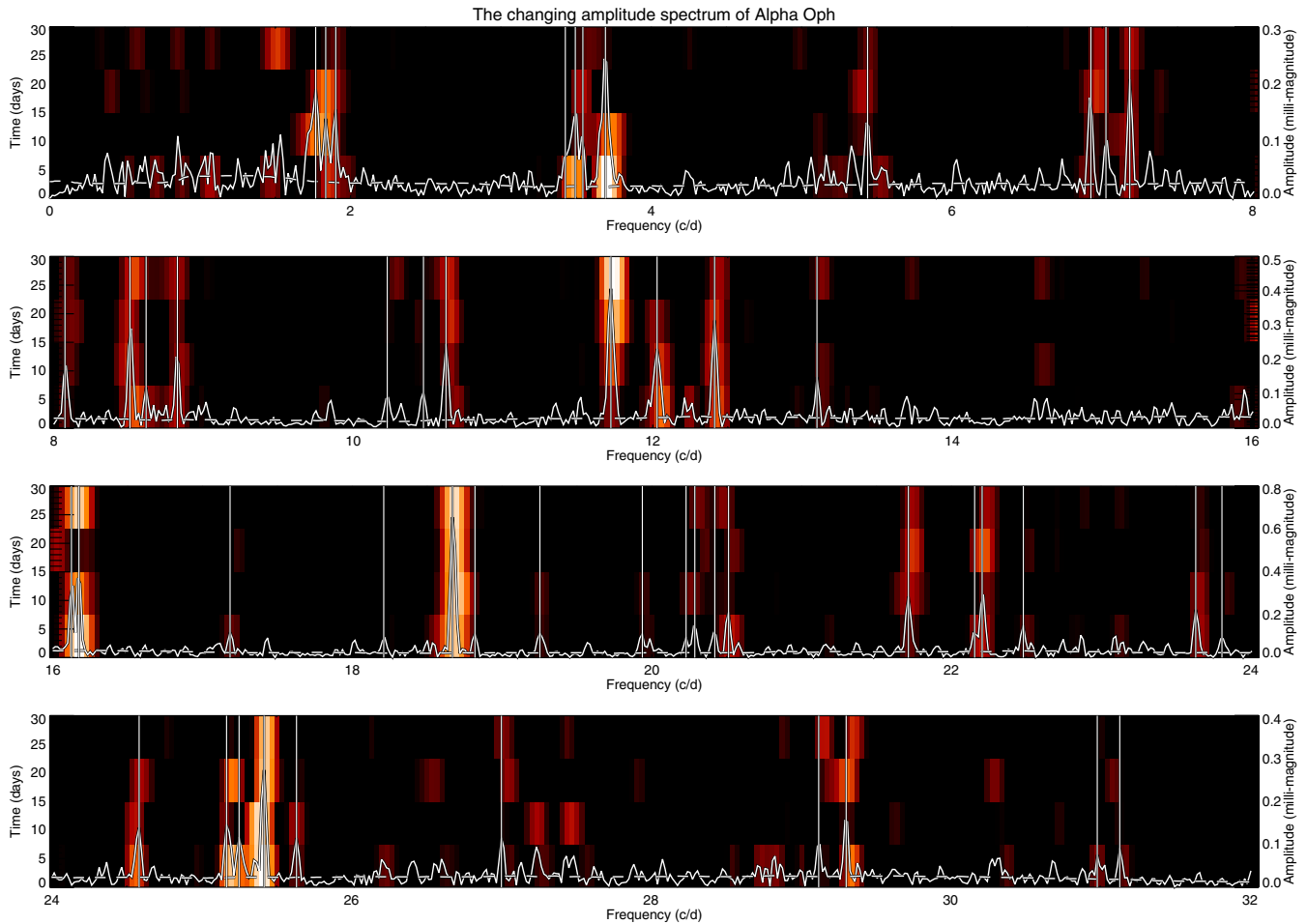
4. ANALYSIS

4.1. Amplitude Spectrum

We have carried out an exhaustive Fourier analysis of the *MOST* photometry. Although the *MOST* data are remarkably complete and evenly spaced compared to ground-based data, we

nonetheless employed a numerical Fourier Transform followed by a "CLEAN"ing step based on the algorithm of Roberts et al. (1987) in order to remove the small sidelobes from the strongest peaks in the power spectrum that arise due to the gaps in the temporal sampling.

Figure 4 shows the amplitude spectrum of our photometry in units of millimagnitude for the range 0–64 c/d. The power for frequencies below ∼ 1 cycle day^{-1} was suppressed by the detrending step described in Section 3. In fact, without detrending, nearly all the frequencies below ∼ 0.75 c/d show significant power above background noise levels. We note that all frequencies up to 1440 c/d were inspected and frequencies

Figure 4. Here, we present our Fourier Analysis of the light curve of α Oph. The solid line shows the amplitude spectrum based on the full 30-day data set with the amplitude labeled on the right-hand axis. Our estimate of the median background noise level is shown with a dashed line and 3.5-σ peaks are shown with vertical lines. Here, we also show the week-by-week temporal variability as a background image of the power spectrum, shown here in logscale. There were no statically significant peaks discovered above 50 c/d.

(A color version of this figure is available in the online journal.)

above 64 c/d are not shown here because no statistically significant peaks were found.

4.2. Non-white "Noise"

It was clear from the power spectrum that the background noise level is higher for frequencies below 30 c/d compared to higher frequencies. In order to properly estimate the statistical significance of a "peak," it is crucial to establish the level of the frequency-dependent noise background. We have used a median filter with a 2 cycles day^{-1} window in order to crudely estimate the background noise power for a given frequency, and this background level is included in Figure 4. We will discuss the physical nature of this non-white noise in Section 5.1; for now we simply treat it as a noise source that can produce spurious spikes in the amplitude spectrum.

4.3. Identification of Distinct Modes

Armed with the frequency-dependent background noise spectrum estimated in Section 4.2, we can now place confidence limits on a given amplitude peak being a "real" distinct pulsation mode rather than having arisen by chance due to background fluctuations. We have chosen a statistical measure such that we only expect one of our identified modes in the range between 0.5 cycle day^{-1} and 64 c/d to be a false positive. Since there are

$\sim$1800 independent frequencies that can be probed in our data in this spectral range, we chose only peaks in the power spectrum above 3.5-σ confidence, a criteria that should produce roughly one false positive assuming pure Gaussian random noise. The 57 modes that survived this analysis are listed in Table 2 and are plotted in Figure 4. We also confirmed the statistical significance of our peaks through a bootstrap analysis, and we note that we would have erroneously identified >500 distinct modes if we had ignored the frequency-dependence of the noise background.

The strongest modes are 18.668 c/d (half-amplitude 0.66 mmag), the closely spaced pair at 16.124/16.174 c/d (0.35/0.41 mmag) and at 11.72 c/d (0.41 mmag). These frequencies are typical for the dominant p-mode oscillations in δ Scuti stars and bear some resemblance to the dominant frequencies observed for another rapid rotator Altair (Buzasi et al. 2005), which had dominant peaks at approximately 15.7, 20.8, and 26.0 c/d. The highest-frequency mode we have detected with high confidence is at 48.35 c/d (0.036 mmag).

Inspection of Figure 4 reveals many additional peaks that appear real—more than can be attributed to random fluctuations of the background. However, we have chosen not to report these peaks in Table 2 in order to maintain a highly pure set of frequencies with minimal false positives. In other words, we understand that many of the other peaks are real pulsational frequencies but
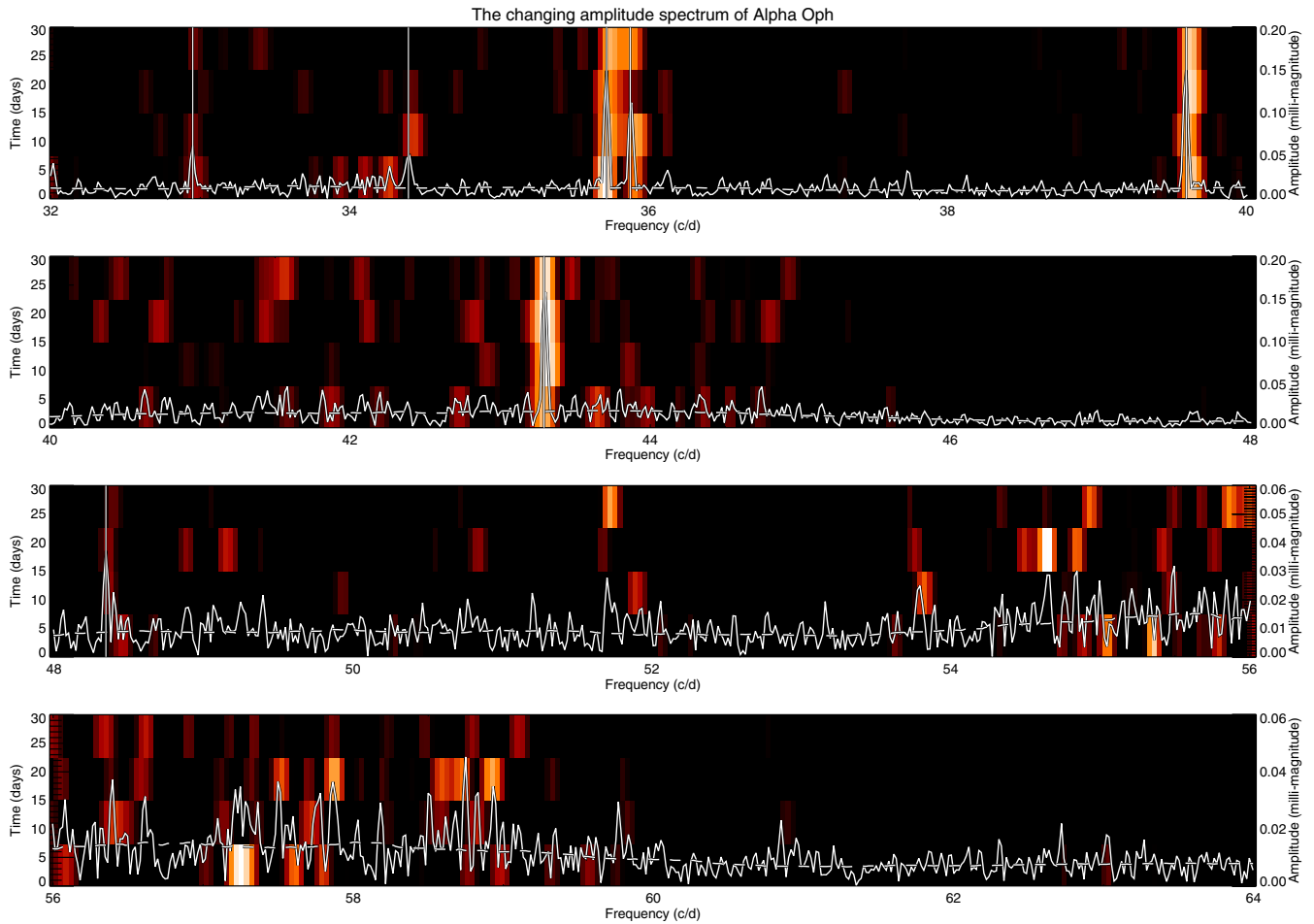
Figure 4. (Continued)

are also sure that some of them are contaminated by background fluctuations. Future mode analysis might allow some of the 2- or 3-σ peaks to become bonafide pulsation frequencies, but we have been conservative in our mode identifications for this paper.

In addition, inspection of the amplitude spectrum at lower frequencies easily reveals increased power at harmonics of 1.7 c/d, close to the expected rotational frequency (1.65 c/d, see Section 2). We will discuss the physical origin of these frequencies in Section 5.

4.4. Time Variability

With such a long data set of high quality, we investigated the stability of the detected modes. Figure 4 contains also the power spectrum split into four 1 week chunks and is depicted as a two-dimensional background image in each panel. One can see the lower-frequency modes, <10 c/d, tend to be variable—strong in some weeks and not present in others. Degroote et al. (2009) found amplitude variability in modes in some higher-mass objects with lifetimes from one to a few days, substantially shorter than those here which tend to be approximately one week. Most of the higher-frequency modes are more stable, although not all. For instance, the 16.1 c/d dominant mode shows amplitude varying by a large amount, consistent with two equal modes with a frequency difference just barely resolved by our 30 day run. The lifetime of modes is another clue to their physical origin and will be discussed in Section 5.

5. DISCUSSION

Here, we wish to discuss three aspects of this data set: the detection of granulation noise <30 c/d, the *p*-mode spectrum, and lastly the discovery of *g*-modes and their rotational modulation.

5.1. Granulation

Poretti et al. (2009) observed the δ Scuti star HD 50844 using COROT, identifying >1000 statistically significant pulsational modes using standard Fourier analysis. Kallinger & Matthews (2010) argued it was physically unreasonable to have so many distinct modes and interpreted the higher power for frequencies lower than ∼30 c/d as due to granulation noise. Indeed, these authors presented a compelling correlation of the granulation cutoff frequency with stellar mass and radius. We subscribe to the interpretation of Kallinger & Matthews, choosing to treat the higher average Fourier power at the lower frequencies as a kind of non-white background noise (see Section 4.2).

In order to better estimate the granulation cutoff frequency, we have plotted the median-filtered power (2 c/d window) in Figure 5. We identified an obvious artifact from the orbital harmonics at 42.6 c/d, and 56.8 c/d and likely present at 14.2 c/d and 28.4 c/d, probably due to imperfect background subtraction of scattered light. By modeling the harmonics beyond 35 c/d, we have crudely estimated the contamination at lower frequencies based on the isolated features at 42.6 and 56.8 c/d. Figure 5 shows our ad hoc model for the contributions from the orbital harmonics and also includes our corrected granulation

Table 2
Distinct Modes Detected for α Oph

Mode No.	Center Frequency (cycles day⁻¹)	Half-amplitude[a] (millimag)	Mode Family[b]
1	1.768 ± 0.017	0.188 ± 0.035	A
2	1.835 ± 0.017	0.135 ± 0.035	
3	1.902 ± 0.017	0.152 ± 0.033	
4	3.428 ± 0.017	0.080 ± 0.024	
5	3.495 ± 0.017	0.160 ± 0.025	A
6	3.545 ± 0.017	0.108 ± 0.024	
7	3.695 ± 0.017	0.268 ± 0.024	B
8	5.439 ± 0.017	0.140 ± 0.028	B
9	6.923 ± 0.017	0.175 ± 0.029	A
10	7.024 ± 0.017	0.101 ± 0.029	
11	7.182 ± 0.017	0.207 ± 0.029	B
12	8.075 ± 0.017	0.183 ± 0.033	
13	8.508 ± 0.017	0.292 ± 0.030	
14	8.617 ± 0.017	0.115 ± 0.028	A
15	8.825 ± 0.017	0.224 ± 0.028	
16	10.227 ± 0.017	0.091 ± 0.023	
17	10.469 ± 0.017	0.104 ± 0.025	
18	10.619 ± 0.017	0.243 ± 0.028	
19	11.720 ± 0.017	0.405 ± 0.033	
20	12.028 ± 0.017	0.228 ± 0.037	A
21	12.412 ± 0.017	0.312 ± 0.039	B
22	13.096 ± 0.017	0.144 ± 0.035	
23	16.124 ± 0.017	0.349 ± 0.039	
24	16.174 ± 0.017	0.411 ± 0.039	
25	17.183 ± 0.017	0.115 ± 0.027	
26	18.209 ± 0.017	0.091 ± 0.025	
27	18.668 ± 0.017	0.655 ± 0.026	
28	18.818 ± 0.017	0.109 ± 0.027	
29	19.252 ± 0.017	0.111 ± 0.026	
30	19.936 ± 0.017	0.109 ± 0.026	
31	20.228 ± 0.017	0.093 ± 0.028	
32	20.286 ± 0.017	0.151 ± 0.027	
33	20.420 ± 0.017	0.120 ± 0.027	
34	20.512 ± 0.017	0.210 ± 0.027	
35	21.713 ± 0.017	0.282 ± 0.032	
36	22.155 ± 0.017	0.117 ± 0.035	
37	22.205 ± 0.017	0.299 ± 0.034	
38	22.480 ± 0.017	0.146 ± 0.037	
39	23.631 ± 0.017	0.223 ± 0.027	
40	23.807 ± 0.017	0.092 ± 0.027	
41	24.582 ± 0.017	0.136 ± 0.027	
42	25.166 ± 0.017	0.144 ± 0.026	
43	25.250 ± 0.017	0.114 ± 0.027	
44	25.416 ± 0.017	0.272 ± 0.027	
45	25.633 ± 0.017	0.111 ± 0.027	
46	27.001 ± 0.017	0.112 ± 0.030	
47	29.120 ± 0.017	0.105 ± 0.029	
48	29.304 ± 0.017	0.172 ± 0.030	
49	30.980 ± 0.017	0.072 ± 0.022	
50	31.130 ± 0.017	0.089 ± 0.022	
51	32.949 ± 0.017	0.060 ± 0.014	
52	34.392 ± 0.017	0.049 ± 0.015	
53	35.718 ± 0.017	0.149 ± 0.015	
54	35.877 ± 0.017	0.113 ± 0.015	
55	39.597 ± 0.017	0.149 ± 0.014	
56	43.292 ± 0.017	0.157 ± 0.022	
57	48.347 ± 0.017	0.036 ± 0.010	

Notes.
[a] Amplitude error derived from level of frequency-dependent noise background (see Section 4.2).
[b] See Section 5.2 for descriptions of g-mode families A and B.

noise spectrum. Here, the granulation cutoff frequency can be estimated to be 26 ± 2 c/d.

As explained in Kallinger & Matthews (2010), the granulation cutoff frequency should be related to the inverse of the sound crossing time of one pressure scale height in the outer convective layer. This leads to a dependence of $\nu_{\text{granulation}} \propto \frac{M}{R^2 T^{\frac{1}{2}}}$. It is beyond the scope of this paper to compare our result with their more elaborate power-law fitting method; however, we can compare our measured granulation cutoff with that predicted by the empirical relation discovered by Kallinger & Matthews (2010, see their Figure 3). Using a mass of 2.18 $M_\odot$, effective radius of 2.7 $R_\odot$, and $T_{\text{eff}} = 8300$ K for α Oph, we find that $M R^{-2} T^{-0.5} \sim 0.25$ (in solar units), leading to an expected $\nu_{\text{granulation}} \sim 300 \mu$Hz = 26 c/d, consistent with our observations.

5.2. Rotationally Modulated g-Modes

Following treatment of Buzasi et al. (2005), we can estimate the frequency of the fundamental radial (p-) mode using the relation

$$P\sqrt{\rho/\rho_\odot} = Q. \tag{1}$$

For $Q = 0.033$ days (Breger 1979) and using the stellar parameters from Table 1, we find $f_{\text{fun}} \sim 10.1$ c/d (compared to 15.6 c/d for the 1.79 $M_\odot$ star Altair). Thus, we will begin by assuming p-modes all have frequencies above or near to this cutoff. A full analysis of the p-modes with tentative mode identifications will be the subject of a future paper. Here, we focus primarily on the unexpected discovery of rotationally modulated g-modes in α Oph.

We showed in Section 4 (see also Figure 2) that there was a ~1 mmag slow (week-timescale) variation seen in the photometry. We also have identified 15 strong modes with frequencies smaller than the fundamental radial mode that cluster around harmonics of 1.7 c/d, close to the rotation frequency. This distinctive structuring suggests we are witnessing the rotational modulation of modes whose frequency in the co-rotating frame is small in comparison to the rotation frequency.

The tabulated frequencies were extracted directly from peaks in the CLEANed Fourier Transform, and we assigned frequency errors based simply on the total length of the data set. We realize that higher precision on the frequency localization of pure modes can sometimes be achieved through a multi-component least-squares fit (e.g., Walker et al. 2005); however, this procedure has convergence problems for very closed spaced frequencies as encountered here. The errors on amplitudes were assigned based on the local background noise as estimated in Section 4.2. We caution that the formal amplitude errors may be underestimated due to non-stationary statistics of the background or due to amplitude variations in the modes themselves. The full time series is available upon request to researchers interested in exploring alternative analysis schemes, but our straightforward approach adopted here leads to conservative errors in the frequencies and is sufficient for the analysis presented here.

Gravity (g-) modes are expected to have long periods compared to p-modes, although it has been difficult to estimate this theoretically for rapid rotators. Indeed, our amplitude spectrum is consistent with a complex and time-variable set of g-modes with co-rotating frequencies ≲0.1 c/d, corresponding to approximately 10 days periods. Normally, the properties of these modes are quite difficult to measure due to the long time frames needed to see the modes travel around the star. However, in our case, the ~1.65 c/d rotational rate of this rapid rotator
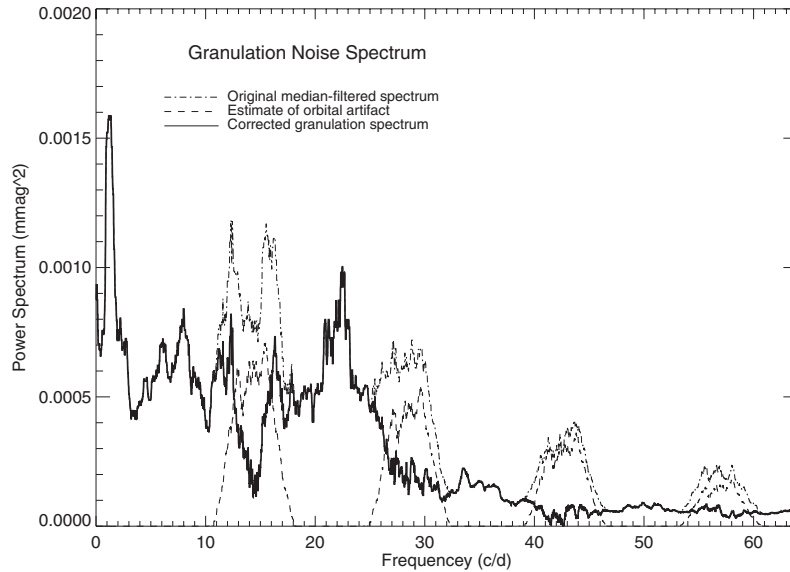
Figure 5. This figure shows the median power spectrum for the light curve of α Oph using a 2 c/d window (dot-dashed line). We note the orbital artifacts at harmonics of 14.2 c/d, and we have crudely estimated the orbital artifact (dashed line). We also plot the corrected granulation spectrum (thick solid line), identifying a clear frequency break at 26 ± 2 c/d.

leads to strong rotational modulation. Note also that modes of north–south asymmetry are invisible to us while the symmetric $l - |m|$ even-parity modes are strongly modulated due to our near equator-on viewing angle.

Specifically, we see small clusters of modes around frequencies ∼1.8, 3.5, 5.4, 7.0, 8.6, 10.4, 12.0 c/d. While some of the higher frequencies here might be *p*-modes, it seems that the strong periodicity at about 1.7 c/d suggests that each cluster represents a new non-radial family of modes with increasing *m* values. Stellar rotation causes light curve variations with frequencies proportional to $mf_{\rm rot}$, since the *m* parameter represents the number of nodes around the equator. With this interpretation, we are seeing non-radial modes corresponding to $m = 1, 2, 3, 4, 5$ and possible $m = 6, 7$. We believe this is the first time such a rich set of *g*-modes has been detected and partially identified around a rapid rotator, although perhaps a related phenomenon may be at work around the late Be star HD 50209 (Diago et al. 2009).

The simultaneous appearance of *g*-modes and *p*-modes would make α Oph a "hybrid" γ Dor-δ Sct pulsator, a class recently explored by Grigahcène et al. (2010) using first Kepler data. Indeed, these authors present a frequency spectrum of KIC9775454 that bears some similarity to the data presented here for α Oph, although our frequency spectrum does not show the characteristic "gap" between 5 and 10 c/d. Further comparison with this work is not possible until more is known about the rotational properties of the Kepler sample, especially since many hybrid pulsators are known to be slowly rotating Am stars.

To further investigate the periodic spacing of the *g*-modes of α Oph, we searched for families of modes that follow a linear frequency relationship of the form

$$f = f_0 + mf_1 \qquad (2)$$

for integer *m*. We found two families, each comprising more than three modes, that can be well represented by this formula. Family A contains five modes; assuming the lowest-frequency mode corresponds to $m = 1$, a least-squares fit gives $f_0 = 0.073 \pm 0.017$ c/d and $f_1 = 1.7095 \pm 0.0002$ c/d. Family B contains four modes, with a fit $f_0 = 0.219 \pm 0.017$ c/d

and $f_1 = 1.7424 \pm 0.0002$ c/d. These modes are noted in Table 2 and included in Figure 6 along with the observed amplitude spectrum for $f < 16$ c/d. There are other solutions that fit three modes or fewer, but in this treatment, we consider just families A and B, since the larger number of modes mean the fit is more reliable and less likely due to chance superpositions.

There are a number of possible interpretations for the linear frequency relationship exhibited by the two mode families, which we shall consider in turn. To first order in the rotation frequency $f_{\rm rot}$, the observed frequency of a mode with radial order *n*, harmonic degree ℓ, and azimuthal order *m* is given by the well-known Ledoux (1951) formula

$$f = f_{n,\ell} + mf_{\rm rot}(1 - C_{n,\ell}). \qquad (3)$$

Here, $f_{n,\ell}$ is the frequency the mode would have in the absence of rotation, and is independent of *m*. The parentheses combine together the effects of the Doppler shift (in transforming from co-rotating to inertial reference frame) and the Coriolis force – the latter represented by the $C_{n,\ell}$ term, which again is independent of *m*. For high-order *g*-modes, $C_{n,\ell}$ approaches $[\ell(\ell + 1)]^{-1}$ (e.g., Aerts et al. 2010).

If we make the identifications $f_0 = f_{n,\ell}$ and $f_1 = f_{\rm rot}(1 - C_{n,\ell})$, then the Ledoux formula is apparently able to explain the linear frequency relationship of the two families, assuming each comprises modes having the same *n* and ℓ but differing *m*. However, there are strong arguments against this conclusion. For both families, the mode frequencies in the co-rotating frame

$$f_{\rm c} \equiv f - mf_{\rm rot} \qquad (4)$$

are small (on the order of 0.1–0.3 c/d) compared to the rotation frequency $f_{\rm rot} = 1.65$ c/d (Table 1). Therefore, the spin parameter $\nu \equiv 2|f_{\rm rot}/f_{\rm c}|$ of the modes must be much larger than unity, implying that their dynamics are dominated by the Coriolis force (see, e.g., Townsend 2003). This represents a fundamental inconsistency with the use of the first-order Ledoux formula (3), which is valid only for $\nu \lesssim 1$.

A possible way around this inconsistency is to relax the assumption that lowest-frequency mode in each family
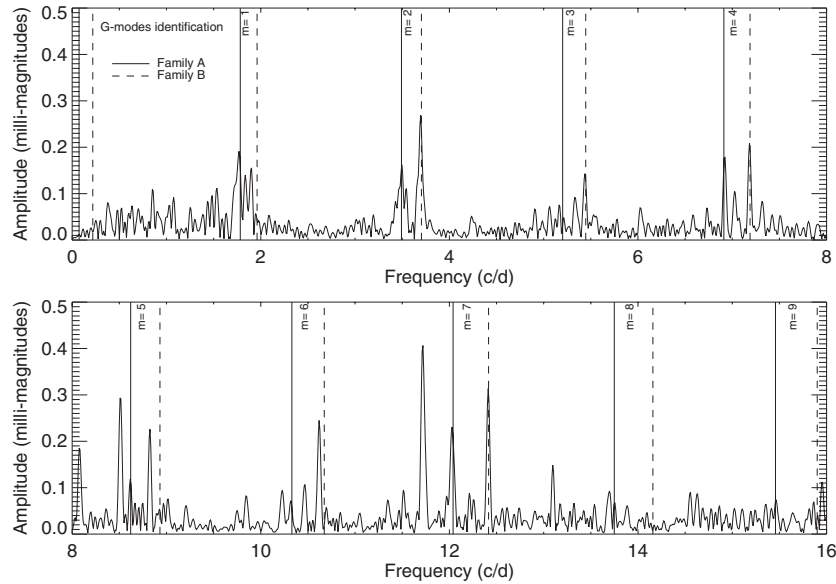
Figure 6. Here, we repeat the amplitude spectrum of the detrended light curve for frequencies below 16 c/d to highlight the *g*-modes. We also include the identifications for two families of modes which are discussed in the text (Section 5.2).

corresponds to azumithal order $m = 1$. If we instead assume $m \geqslant 3$ for these modes, then by Equation (4)[6] we can achieve $\nu \lesssim 1$. However, this "fix" itself runs into difficulty when we note that for both mode families $f_1 > f_{\rm rot}$, implying that the Coriolis coefficients $C_{n,\ell}$ are negative. This is incompatible with the above-mentioned limit $C_{n,\ell} \approx [\ell(\ell+1)]^{-1} > 0$ (indeed, we are not aware of any physically plausible pulsation model that predicts negative Coriolis coefficients).

Accordingly, we are led to abandon the Ledoux formula as an explanation for the linear frequency relationship of the two mode families. In searching for alternative interpretations, we note that the small magnitude of f_0 suggests we may be observing seven *dispersion-free* low-frequency modes. In rotating stars, there are two classes of mode that are dispersion free: equatorial Kelvin modes (which are prograde) and Rossby modes (which are retrograde). Rossby modes tend not to generate light variations because they are incompressible, so let us put them aside for the moment (although not forget about them completely).

Focusing therefore on the Kelvin modes, these are prograde sectoral ($\ell = m$) *g*-modes which are confined to an equatorial waveguide by the action of the Coriolis force (see Townsend 2003). A defining characteristic of these modes is that their frequencies are directly proportional to *m*. At high radial orders, these frequencies in the co-rotating frame can be approximated by

$$f_{\rm c} \approx \frac{m I_{\rm g}}{2\pi^2 n};$$ (5)

here, following Mullan (1989), we define

$$I_{\rm g} = \frac{1}{\sqrt{2}\pi^2} \int_0^\infty \frac{N}{r} \, dr,$$ (6)

with N is the Brunt-Väisälä frequency. The corresponding observed frequencies are then given by

$$f \approx m \left(\frac{I_{\rm g}}{2\pi^2 n} + f_{\rm rot} \right).$$ (7)

---

[6] We note that negative $f_{\rm c}$ values in this equation indicate modes whose phase propagation in the co-rotating frame is retrograde.

For a group of modes all having the same *n*, this expression predicts a linear frequency relationship *with zero intercept*. If *n* varies within the group, however, then there will be some scatter about a linear relationship, with a relative amplitude of $\sim \Delta n/n$.

To examine whether the two mode families could be Kelvin modes, we re-fit their frequencies assuming a zero intercept (again identifying the lowest-frequency mode as $m = 1$). This gives $f_c/m = 0.07 \pm 0.03$ c/d for family A and $f_c/m = 0.10 \pm 0.03$ c/d for family B. To interpret these values, we assume a relationship $I_{\rm g} \approx 10^{-3}\sqrt{(M/M_\odot)/(R/R_\odot)^3}$ Hz, derived from the $n = 3$ polytropic model considered by Mullan (1989). Using the stellar parameters from Table 1, this yields $I_{\rm g} \approx 34$ c/d. Hence, the approximate radial orders of the modes are derived as $n \approx 24$ (family A) and $n \approx 17$ (family B), with corresponding scatter (based on the quoted uncertainties in the f_c/m fits) of $\Delta n \approx 10$ and $\Delta n \approx 5$, respectively.

These values are consistent with the typical radial orders of unstable *g*-modes observed in the more-massive Slowly Pulsating B (SPB) stars (e.g., Cameron et al. 2008; Pamyatnykh 1999). This lends strong support to the identification of the two mode families as high-order ($n \approx 17$ and $n \approx 24$) *g*-modes transformed by the Coriolis force into equatorial Kelvin modes.

As a last comment, according to Figure 4, most of the *g*-modes seem to be time-variable within our one month time frame, in contrast to the *p*-modes whose amplitudes are more typically constant within the errors. The *g*-modes tend to change on a timescale similar to the intrinsic mode period (~ 10 days) or a bit longer. This could be due to superposition of many closely spaced modes in what appears to be indeed a complex spectra. Alternatively, many excitable modes may be transferring energy between themselves, leading to a dynamic and time-variable amplitude spectrum. The ability to see so many independent *l*- and *m*-modes by using strong rotational modulation is invaluable to deriving strong constraints on the mode properties up to high order (here up to $m = 7$) and promises to reveal interior stellar structure with additional analysis.

6. CONCLUSIONS

This first long stare by *MOST* at a rapidly rotating A star has led to number of a new results. We detect for the first

time a rich *p*-mode spectrum consistent with low-amplitude *δ* Scuti pulsations, and measure a granulation spectrum below 26 ± 2 c/d. In total, we have identified 57 ± 1 distinct modes below 50 c/d including a complex set of low-frequency modes that we identify as rotationally modulated *g*-modes with (co-rotating) frequencies ~ 0.1 c/d. A mode analysis revealed linear relationships between the spacings of *g*-modes up to $m = 7$, an unexpected result for a star rotating at $\sim 90\%$ of breakup. This periodicity can be explained as due to dispersion-free equatorial Kelvin waves (prograde $l = m$-modes) although some inconsistencies in our analysis demand follow-up study. Lastly, the long time-base has allowed us to study the mode lifetime, finding that most *p*-modes are stable while *g*-modes appear to live only a few times their intrinsic (co-rotating) periods.

Understanding the effect of rapid rotation on stellar interiors is crucial to developing reliable models for massive star evolution in general. *α* Oph is emerging as a crucial prototype object for challenging our models and to spur observational and theoretical progress. Additional work is planned using adaptive optics to determine the mass of the star by measuring the 8 year visual orbit more precisely, using visible and infrared interferometry to strictly constrain possible differential rotation and gravity darkening laws, and using asteroseismology to follow up on the new discoveries outlined here.

Facility: MOST, CHARA (MIRC)

REFERENCES

Aerts, C., Christensen-Dalsgaard, J., & Kurtz, D. W. 2010, Asteroseismology (Berlin: Springer)
Barban, C., et al. 2007, A&A, 468, 1033
Breger, M. 1979, PASP, 91, 5
Buzasi, D. L., et al. 2005, ApJ, 619, 1072
Cameron, C., et al. 2008, ApJ, 685, 489
Cunha, M. S., et al. 2007, A&AR, 14, 217
Cutri, R. M., et al. 2003, VizieR Online Data Catalog, 2246, 0
Degroote, P., et al. 2009, A&A, 506, 471
Demarque, P., Woo, J., Kim, Y., & Yi, S. K. 2004, ApJS, 155, 667
Diago, P. D., et al. 2009, A&A, 506, 125
Domiciano de Souza, A., Kervella, P., Jankov, S., Abe, L., Vakili, F., di Folco, E., & Paresce, F. 2003, A&A, 407, L47
Erspamer, D., & North, P. 2003, A&A, 398, 1121
Gatewood, G. 2005, AJ, 130, 809
Gray, R. O., Napier, M. G., & Winkler, L. I. 2001, AJ, 121, 2148
Grigahcène, A., et al. 2010, ApJ, 713, L192
Hinkley, S., et al. 2010, ApJ, in press
Jackson, S., MacGregor, K. B., & Skumanich, A. 2005, ApJS, 156, 245
Kallinger, T., & Matthews, J. M. 2010, ApJ, 711, L35
Kallinger, T., et al. 2008a, A&A, 478, 497
Kallinger, T., et al. 2008b, Commun. Asteroseismol., 153, 84
Kim, Y., Demarque, P., Yi, S. K., & Alexander, D. R. 2002, ApJS, 143, 499
Ledoux, P. 1951, ApJ, 114, 373
Lee, U., & Saio, H. 1997, ApJ, 491, 839
Maeder, A., & Meynet, G. 2000, ARA&A, 38, 143
Matthews, J. M. 2007, Commun. Asteroseismol., 150, 333
Matthews, J. M., Kusching, R., Guenther, D. B., Walker, G. A. H., Moffat, A. F. J., Rucinski, S. M., Sasselov, D., & Weiss, W. W. 2004, Nature, 430, 51
Monnier, J. D., Berger, J., Millan-Gabet, R., & ten Brummelaar, T. A. 2004, Proc. SPIE, 5491, 1370
Monnier, J. D., et al. 2006, Proc. SPIE, 6268, 55
Monnier, J. D., et al. 2007, Science, 317, 342
Mullan, D. J. 1989, ApJ, 337, 1017
Pamyatnykh, A. A. 1999, Acta Astron., 49, 119
Perryman, M. A. C., et al. 1997, A&A, 323, L49
Pinsonneault, M. 1997, ARA&A, 35, 557
Poretti, E., et al. 2009, A&A, 506, 85
Reegen, P., et al. 2006, MNRAS, 367, 1417
Reese, D., Lignières, F., & Rieutord, M. 2008, A&A, 481, 449
Rieutord, M. 2006, A&A, 451, 1025
Roberts, D. H., Lehar, J., & Dreher, J. W. 1987, AJ, 93, 968
Roxburgh, I. W. 2006, A&A, 454, 883
ten Brummelaar, T. A., et al. 2005, ApJ, 628, 453
Townsend, R. H. D. 2003, MNRAS, 340, 1020
van Belle, G. T., Ciardi, D. R., Thompson, R. R., Akeson, R. L., & Lada, E. A. 2001, ApJ, 559, 1155
von Zeipel, H. 1924a, MNRAS, 84, 665
von Zeipel, H. 1924b, MNRAS, 84, 684
Walker, G., et al. 2003, PASP, 115, 1023
Walker, G. A. H., et al. 2005, ApJ, 635, L77
Walker, G. A. H., et al. 2008, A&A, 482, 691
Yi, S., Demarque, P., Kim, Y., Lee, Y., Ree, C. H., Lejeune, T., & Barnes, S. 2001, ApJS, 136, 417
Zhao, M., et al. 2009, ApJ, 701, 209